Ocean Engineering 94 (2015) 36–50

Contents lists available at ScienceDirect

Ocean Engineering

journal homepage: www.elsevier.com/locate/oceaneng

Influence of wall proximity on flow around two tandem circular cylinders

X.K. Wang [a,*], J.-X. Zhang [b], Z. Hao [c], B. Zhou [a], S.K. Tan [a]

[a] Maritime Research Centre, Nanyang Technological University, 639798, Singapore
[b] School of Naval Architecture, Ocean and Civil Engineering, Shanghai Jiao Tong University, Shanghai 200240, China
[c] College of Logistics Engineering, Shanghai Maritime University, Shanghai 201306, China

ARTICLE INFO

Article history:
Received 3 August 2013
Accepted 30 November 2014
Available online 16 December 2014

Keywords:
Tandem cylinders
Wall proximity
Vortex shedding
Drag and lift coefficients
Spectrum of lift coefficient
Particle image velocimetry (PIV)

ABSTRACT

An experimental study was conducted to investigate the flow around two tandem cylinders placed near and parallel to a plane wall. The Reynolds number based on the cylinder diameter (D) was 6300. The cylinder centre-to-centre spacing ratio ($L^*=L/D$) was varied from 1.5 to 6, and the gap-height-to-cylinder-diameter ratio ($G^*=G/D$) from 0.15 to 2. The flow fields were measured using Particle Image Velocimetry (PIV), in conjunction with measurements of fluid dynamic forces (drag and lift) on the downstream cylinder using load cell. The flow strongly depends on the combined value of G^* and L^*. With reference to G^*, the flow could be classified as vortex-shedding suppression regime ($G^*<0.3$), intermediate-gap regime ($0.3<G^*<1$) where vortex shedding occurs but is influenced by wall proximity, and large-gap regime ($G^*>1$) where the wall influence becomes negligible. Similarly, three categories can be identified as a function of L^*, namely, extended-body regime $1<L^*<2$, reattachment regime at $2<L^*<4$, and impinging regime at $L^*>4$. Variations of dynamic drag and lift coefficients, spectra, Strouhal numbers, and Reynolds shear stress are also presented to characterize the different flow regimes in the G^*–L^* plane.

1. Introduction

The interference of flow around two circular cylinders is of both academic interest and practical importance, see Sumner (2010) for a comprehensive review. Among the many possible arrangements of the two cylinders to be positioned in relative to the flow direction, the tandem configuration has been extensively studied. This type of interference, referred to as 'wake interference' by Zdrvkovich (1987), is a function of the inter-cylinder distance (expressed as the ratio between the centre-to-centre spacing and the cylinder diameter, $L^*=L/D$, thereafter abbreviated as the spacing ratio). Zdravkovich (1987) proposed that the flow can be classified into three basic types: (i) single bluff-body regime at small L^* ($1<L^*<1.2\sim1.8$), where periodic von Kármán vortex shedding is observed only in the wake of the downstream cylinder; (ii) reattachment regime at moderate L^* ($1.2\sim1.8<L^*<3.4\sim3.8$), where the shear layers emanating from the upstream cylinder reattach onto the surface of the downstream cylinder; (iii) impinging regime at large L^* ($L^*>3.4\sim3.8$), where von Kármán vortices are shed from the upstream cylinder and periodically impinge on the downstream cylinder. Zhou and Yiu (2006) showed that the reattachment regime ($2<L^*<5$) can be further sub-divided into two distinct categories, for which the reattachment is on the rear and leading surfaces of the downstream cylinder, respectively (see Fig. 1). The exact values of L^* to delineate the boundaries between different regimes depend on the value of Reynolds number (Carmo et al., 2010) and free-stream turbulence intensity (Ljungkrona et al., 1991). The critical spacing ratio (L^*_{cr}), at which periodic vortex shedding begins to occur from the upstream cylinder, varies from $L^*_{cr}=3$ to 5 in the literature (e.g., Lee et al., 2009). Correspondingly, the fluid forces on the cylinders would experience a discontinuous 'jump' at about L^*_{cr} (Zdravkovich and Pridden, 1977). Moreover, Xu and Zhou (2004) showed that the vortex shedding frequency is dependent on Reynolds number over the range $Re=800–4.2\times10^4$ ($Re=UD/\nu$, where ν is the kinematic viscosity of fluid).

On the other hand, there are a number of engineering practices in which cylindrical structures are placed near a plane wall, such as submarine pipelines, risers and cables on seabed. To date, many researchers have examined the influence of wall proximity on a single cylinder with the cross-section of either circular (e.g., Bearman and Zdravkovich, 1978; Lei et al., 1999; Price et al., 2002; Dipankar and Sengupta, 2005; Nishino et al., 2007; Wang and Tan, 2008a; Lin et al., 2009; Sarkar and Sarkar, 2010; Ong et al., 2012; Wang et al., 2013), square (e.g., Wang and Tan 2008b; Mahir, 2009) or rectangular (e.g., Maiti, 2012; Maiti and Bhatt, 2014). The nearby wall affects not only the dynamic pressure and forces on the

* Corresponding author. Tel.: +65 67906619; fax: +65 67906620.
E-mail address: cxkwang@ntu.edu.sg (X.K. Wang).

http://dx.doi.org/10.1016/j.oceaneng.2014.11.018
0029-8018/

cylinder, but also the wake pattern and flow-induced vibrations. The ratio between the gap height to the cylinder diameter ($G^*=G/D$, abbreviated hereafter as the gap ratio) is found to be the predominant parameter. The impermeability of the wall poses an irrotational constraint to the wake development, resulting in suppression of the classical von Kármán vortex shedding that is in absolute instability (Huerre and Monkewitz, 1990) below a critical gap ratio (G^*_{cr}). As sketched in Fig. 2(a), when $G^* < G^*_{cr}$, the wake is steady with a long recirculation region: while the gap flow keeps attached on the wall, the upper shear layer emanating from the cylinder exhibits as elongated Kelvin-Helmholtz (K-H) type of roll-ups (in convective instability). However, when $G^* > G^*_{cr}$ (Fig. 2(b)), the gap flow is strong enough to detach upward from the wall (or upwash), and to interact with the upper shear layer to form discrete vortices. It should be noted that the vortex shedding is asymmetric about the horizontal wake centerline; also, there is a coupling between the lower shear layer and the wall boundary layer, as reflected by the phenomenon that each anticlockwise vortex is accompanied by a small clockwise vortex in the near wall region. The value of $G^*_{cr} \approx 0.3$ slightly varies with Re and thickness of the wall boundary layer (e.g., Buresti and Lanciotti, 1992; Price et al., 2002).

However, little attention has been paid to the configuration of two tandem cylinders in proximity to a plane wall (see Fig. 3). The flow interference between the two cylinders is further complicated due to the presence of the wall boundary. Bhattacharyya and Dhinakaran (2008) numerically studied the 2-dimensional (2D) flow around two tandem square cylinders with a linear incident velocity profile at $G^*=0.5$ and $L^*=1.5$–6. The non-uniform approach flow causes difference in the strength of the upper and lower shear layers. The flow can be steady up to Re=125 depending on the value of L^*. More recently, Harichandan and Roy (2012) simulated the flow around two near-wall tandem cylinders (circular/square) at Re=100 and 200, $G^*=0.5$ and 1, and $L^*=2$ and 5. For a given Re, the Strouhal numbers of the two cylinders are identical, but the lift and drag coefficients are different.

As described above, there is limited information available on the flow around two tandem cylinders in proximity to a wall boundary. Two aspects need attention. Firstly, the only two published studies, namely, Dhinakaran (2008) and Harichandan and Roy (2012), were conducted at relatively low Re (up to 200), that is, in the laminar regime. Yet, in engineering practice the flow is generally in the subcritical regime. Secondly, both studies considered only a rather limited number of combinations of G^* and L^*, and hence a complete picture in the G^*–L^* plane is still unavailable. These motivate the present relatively systematic investigation for $0.15 \le G^* \le 2$ and $1.5 \le L^* \le 7$ under a constant Reynolds number in subcritical regime (Re=6300).

2. Experimental set-up and methodology

The experiments were performed in a re-circulating open channel located at Maritime Research Centre, Nanyang Technological University, with a test section of 5 m × 0.3 m × 0.45 m (length × width × height). The channel bed and the two side walls of the test section were made of glass to allow for optical access. The free-stream velocity was uniform to within 1.5% across the test section, and the turbulence intensity in the free stream was below 2%.

Fig. 3 shows a sketch of the two tandem cylinders placed near and parallel to a plane wall. The cylinder models were made of smooth, transparent acrylic rod with an outer diameter of $D=15$ mm. During the experiments, the free-stream velocity was kept constant at $U=0.42$ m/s (Re=6300). The approach boundary layer was fully developed with a thickness of $\delta=7$ mm ($\sim 0.5D$). The cylinders' centre-to-centre spacing was varied as $L=22.5$, 30, 45, 60, 75, 90 and 105 mm ($L^*=1.5$–7), and the gap height $G=2.25$, 6, 9, 12, 21 and 30 mm ($G^*=0.15$–2). Therefore, totally 42 cases were considered in the present study.

The span (b) of the cylinders was 200 mm, leading to an aspect ratio (AR) of $b/D=13.3$. This value was considered to be large enough (AR ≥ 10 according to previous finding, for example, Lam and Zou, 2010) to ensure a nominally 2D flow in the near wake. Therefore, the velocity measurements with Particle Image Velocimetry (PIV) were performed in the mid-span plane. The origin of the coordinate system was located at the center of the upstream cylinder, with x, y and z denoting the streamwise, transverse and spanwise directions, respectively. The positive drag and lift forces are in the x- and y-directions, respectively.

Velocity measurements were performed using a digital PIV system (LaVision model). The flow field was illuminated with a double cavity Nd:YAG laser light sheet at 532 nm wavelength (Litron model, power~135 mJ per pulse, duration~5 ns). Spherical® 110P8 hollow glass spheres (neutrally buoyant with a mean diameter of 13 μm) were seeded in the flow as tracer particles. The images were

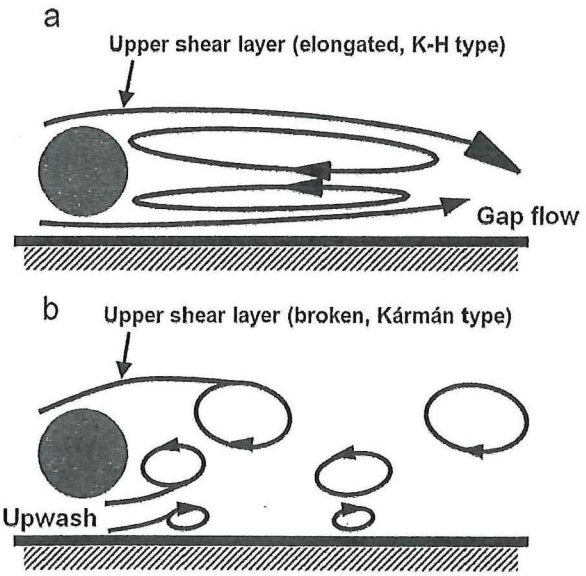

Fig. 2. Schematic of the flow around a near-wall single cylinder: (a) vortex-shedding-suppression regime at small gap ratio; and (b) vortex-shedding regime at moderate gap ratio. Proposed based on the flow measurement results in Wang and Tan (2008a).

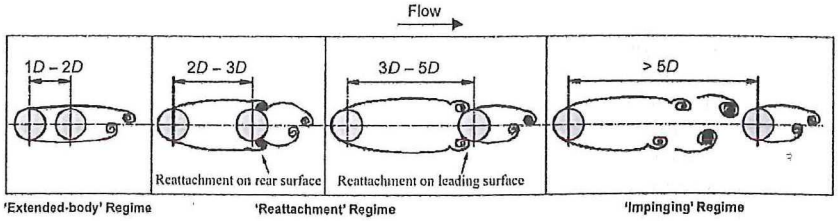

Fig. 1. Schematic of the flow around two tandem cylinders as a function of spacing ratio (L^*) under free-standing conditions. Modified from Zhou and Yiu (2006).

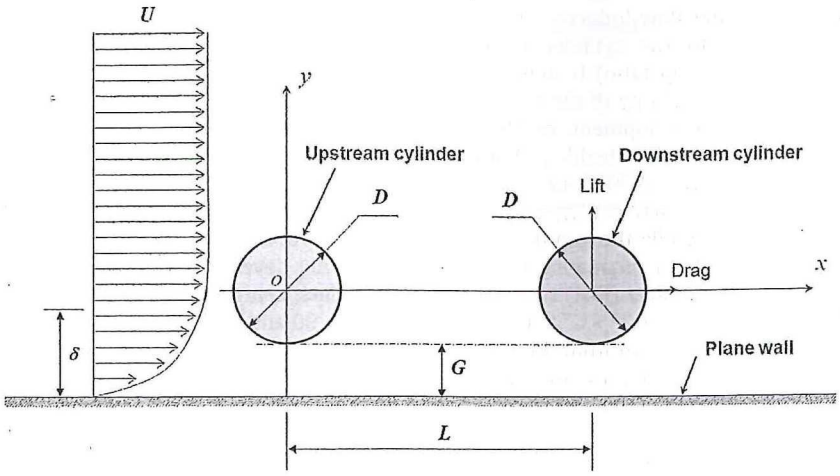

Fig. 3. Schematic of the flow around two near-wall tandem cylinders.

recorded using a 12-bit CCD camera with a resolution of 1600 × 1200 pixels. LaVision Davis software (Version 7.2) was used to process the particle images and determine the velocity vectors. Particle displacement was calculated using the fast-Fourier-transform (FFT) based cross-correlation algorithm with standard Gaussian sub-pixel fit structured as an iterative multi-grid method. The processing procedure included two passes, starting with a grid size of 64 × 64 pixels, stepping down to 32 × 32 pixels overlapping by 50%, which resulted in a set of 7500 vectors (100 × 75) for a typical field. In between the two passes, the vector maps were filtered by using a 3 × 3 median filter in order to remove possible outliers. The number of particles in a 32 × 32 pixel window was of the order of 10~15 to yield strong correlations. The field of view was set at 190 mm × 143 mm, therefore the spatial resolution was 1.9 mm × 1.9 mm (i.e., 0.13D × 0.13D). For each case, a series of 1050 instantaneous flow fields was acquired at the sampling frequency of 15 Hz (or 70 s recordings), in order to achieve a reasonably statistical convergence of the measured quantities, such as Reynolds shear stress. The uncertainty in the instantaneous velocities (u and v) was estimated to be about 3.5% for the present setup. The instantaneous spanwise vorticity ($\omega_z = \Delta v/\Delta x - \Delta u/\Delta y$) was calculated using the least squares extrapolation scheme. The uncertainty in ω_z was estimated to be about 10% based on the method proposed by Fouras and Soria (1998).

A piezoelectric load cell (Kistler Model 9317B) was used to directly measure the fluid dynamic forces on the downstream cylinder, drag (F_D) and lift (F_L). The output signal was captured with a National Instruments A/D card at a sampling rate of 100 Hz (at least 1 order of magnitude greater than the vortex shedding frequency, which was about 5–6 Hz). The duration of recording for each case was about 200 s, which corresponded to about 1000 cycles of vortex shedding and was sufficiently long according to the criterion proposed by Sakamoto et al. (1987). The dimensionless shedding frequency was expressed as Strouhal number ($St = fD/U$), where f is the frequency determined from spectral analysis of the fluctuating lift coefficient using power spectral density (PSD) function. Also, the mean and root-mean-square (RMS) values of fluid dynamic drag and lift coefficients ($C_D = 2F_D/\rho U^2 Db$ and $C_L = 2F_L/\rho U^2 Db$) were calculated, where ρ is the fluid density. Through a number of repeated measurements on a single cylinder, the uncertainty in the mean drag was determined to be within 1%. The data for a free-standing (isolated) single cylinder measured at the same Reynolds number (Re=6300) served as the benchmark reference: $\overline{C}_{D0} = 1.1$, $C'_{D0} = 0.055$, $C'_{L0} = 0.075$ and $St_0 = 0.2$ (where the subscript 0 denotes the isolated cylinder).

3. Results and discussion

3.1. Near-wall single cylinder

The effects of wall proximity on a single cylinder has been examined in this section. Fig. 4 shows the variation of the dynamic force coefficients ($\overline{C}_D$, $\overline{C}_L$, C'_D and C'_L) versus G^*, together with the data reported by Roshko et al. (1975) and Lei et al. (1999). As shown in Fig. 4(a), a prominent feature is that the most dramatic change of $\overline{C}_D$ occurs from small- to intermediate-gap ratios (e.g., $G^* < 0.75$); when $G^* > 1$, by contrast, it remains approximately constant at $\overline{C}_D \approx 1.1$ (asymptotically approaching the value for an isolated cylinder), indicating that the wall effects become negligible. A similar trend is found for the RMS coefficients (C'_D and C'_L) as shown in Fig. 4(c). However, it is noted that the asymptotic values are considerably lower than those reported in Roshko et al. (1975) and Lei et al. (1999), namely, $\overline{C}_D \approx 1.1$ versus 1.3 and $C'_L \approx 0.075$ versus 0.6. The discrepancy is likely attributed to the difference in measurement techniques and oncoming flow conditions (such as Re and δ). Note the data in Roshko et al. (1975) and Lei et al. (1999) were based on pressure distribution around the cylinder circumference for an elemental slice (referred to as *sectional force* by Norberg (2003)), while the present study measured the *total force* on the whole span of the cylinder, which always has a lower magnitude due to the end effects (West and Apelt, 1997). In the present study, the thickness of boundary layers developed on the side walls where the two ends of the cylinder were attached was about 0.5D, so the length of the cylinder subjected to end effects was about 1D (or 7.5% of the total span). Therefore, the difference between the measured total force and the ideal sectional force would be less than 10%. In fact, the present results are in good agreement with the published data on a single cylinder using similar measurement technique (load cell), such as $\overline{C}_D \approx 1.186$ and $C'_L \approx 0.089$ in Lam et al. (2003) for Re=4.8×10^4, and $C'_L \approx 0.08$ in Tadrist et al. (1990) for Re=7000. As depicted in Fig. 4(b), the cylinder experiences a positive mean lift ($\overline{C}_L > 0$) at small- to intermediate-G^*, suggesting that the cylinder is pushed upward from the wall. The mean lift coefficient has a maximum of $\overline{C}_L \approx 0.3$ at the smallest gap ratio ($G^* = 0.15$), and thereafter decreases monotonically until reaching the asymptotic value of $\overline{C}_L = 0$ at $G^* > 1$.

Fig. 5(a) shows the time histories of dynamic lift coefficient (C_L) on the cylinder at different gap ratios. As G^* increases, the signal changes from a chaotic pattern at $G^* = 0.15$ and 0.25, to a periodic pattern at $G^* > 0.4$ with a much higher magnitude of fluctuation. The chaotic pattern at small-G^* is due to the cessation of periodic

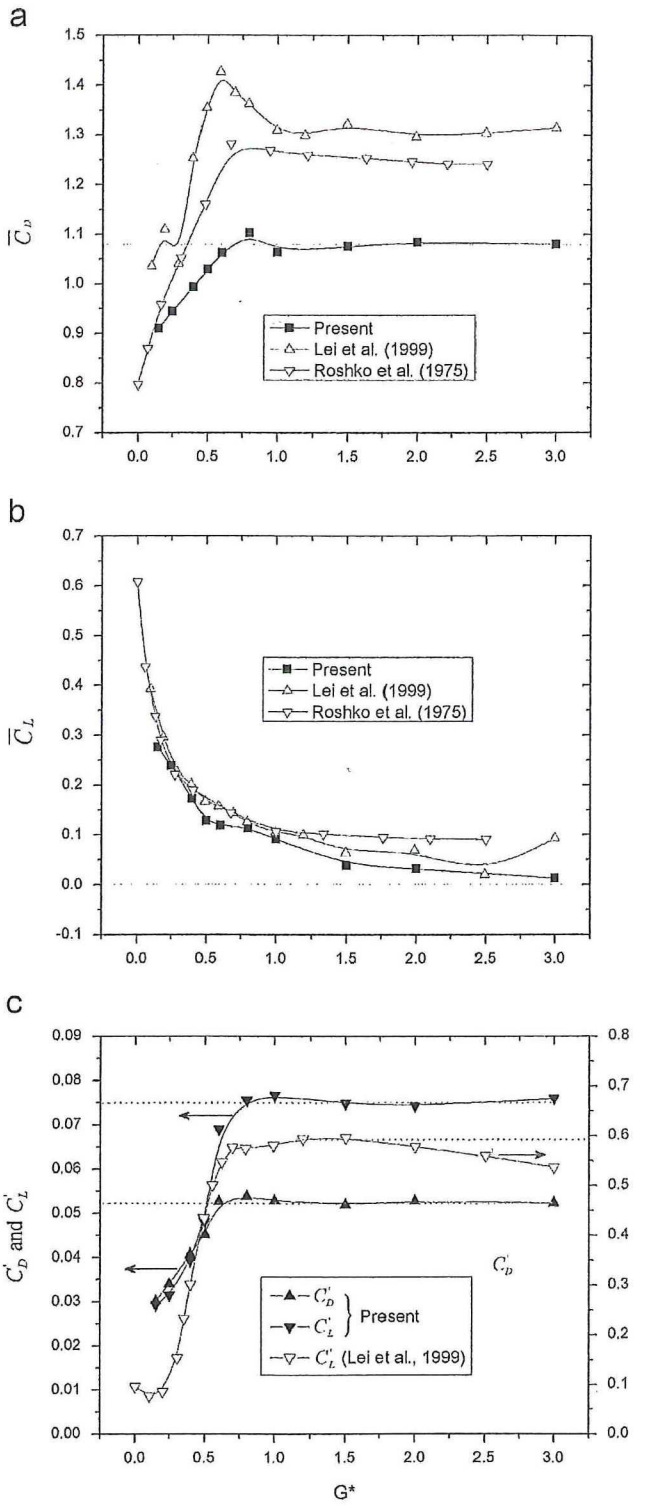

Fig. 4. Variation of dynamic force coefficients with G^* for the near-wall single cylinder: (a) mean drag coefficient ($\overline{C}_D$); (b) mean lift coefficient ($\overline{C}_L$); and (c) RMS drag (C_D') and lift (C_L') coefficients. Present: Re=6300 and δ=0.5D; Lei et al. (1999): Re=1.36 × 10^4 and δ=0.14D; Roshko et al. (1975): Re=2 × 10^4 and δ=0.5D.

vortex shedding from the cylinder (e.g., Price et al., 2002; Wang and Tan, 2008a). Also, the critical gap ratio (G^*_{cr}) is between 0.25 and 0.4, in accordance with the reported value of $G^*_{cr} \approx 0.3$ in the literature. The periodicity of lift signals is reflected in the corresponding spectra shown in Fig. 5(b). For $G^* \geq 0.4$, each spectrum displays one obvious peak at St ≈ 0.2 (similar to the case of an isolated cylinder), with the magnitude of the peak progressively increasing with G^* until G^*=0.8. This indicates that vortex shedding becomes stronger within this range (a similar trend is inferred from the velocity data in Wang and Tan (2008a)). At G^*=0.15 or 0.25, on the other hand, a weak peak is discernible at a relatively high frequency, that is, St ≈ 0.85, which corresponds to the K-H roll-ups in shear layer instability. Rajagopalan and Antonia (2005) proposed an empirical relationship between the shear layer instability frequency (f_{sl}) and the vortex shedding frequency (f_V) as a function of Re for an isolated cylinder, namely, $f_{sl}/f_V = 0.029 \times Re^{0.65}$. The predicted value using this equation for Re=6300 is f_{sl}/f_V=8.55, which is about twice the measured value of 0.85/0.2=4.25. However it is noted that the working fluid in Rajagopalan and Antonia (2005) is air (vs. water in the present study), which would result in relatively thinner shear layers and hence higher f_{sl}, since f_{sl} is inversely proportional to the shear layer thickness (Gerrard, 1967). Fig. 5(b) also shows that at G^*=0.4 (corresponding to onset of periodic vortex shedding), the spectrum exhibits co-existence of both peaks (St ≈ 0.2 and 0.85), albeit rather weak, implying a transition/competition between the two types of instability (von Kármán vs. K-H).

3.2. Near-wall tandem cylinders

3.2.1. Instantaneous flow patterns around the cylinders

Fig. 6 shows a representative snapshot of the instantaneous vorticity fields around the near-wall tandem cylinders at selected gap ratios (G^*=0.15, 0.4, 0.6 and 1.4) and spacing ratios (L^*=2, 3 and 5). It is obvious that the flow patterns depend on both G^* and L^*. Periodic vortex shedding from both cylinders is suppressed when G^* is small. For G^*=0.15 (1st row), the upper shear layer emanating from the upstream cylinder is K-H type of roll-ups (elongated in the streamwise direction with negative vorticity), which pass over (or overshoot) the downstream cylinder. However, the lower shear layer, which is evident in the spacing between the cylinders, is rather weak in magnitude and small in size. For G^*=0.4 (2nd row), both shear layers are still largely in K-H type at small spacing ratios (e.g., L^*=2 or 3). At L^*=5, on the other hand, they begin to display as relatively large, discrete 'patches' of vorticity behind the downstream cylinder, indicative of the occurrence of vortex shedding. However, no vortex shedding is observed from the upstream cylinder: while the upper shear layer is still in K-H type, the lower shear layer either reattaches steadily on the leading surface of the downstream cylinder at L^*=2 and 3, or dissipates around $x/D \approx 4$ at L^*=5. In addition, flow-induced separation is found in the near wall region, similar to the case of the near-wall single cylinder shown in Fig. 2(b). When G^* increases to 0.6 (3rd row), the wall effects still exist, but to a lesser degree. At this gap ratio, periodic vortex shedding is always observed from the downstream cylinder, as well as from the upstream cylinder at wide-spacing ratios (e.g., L^*=5). At G^*=1.4 (4th row), the wall effects become almost negligible such that the flow is similar to the free-standing case. Obviously, the three cases, L^*=2, 3 and 5, belong to the 'extended-body', 'reattachment' and 'impinging' regimes, respectively, as shown in Fig. 1. The critical spacing ratio is $L^*_{cr} \approx 4.5$, which is also consistent with the reported values of L^*_{cr}=3–5 in the literature.

A closer examination of the instantaneous vorticity fields indicates that the effects of wall proximity cannot simply be described as inhibiting vortex shedding from the cylinders; instead, it plays a complex role in affecting the shear layer development and interaction. Take the case of L^*=2 at different gap ratios (left column in Fig. 6) as an example. At G^*=1.4, the flow is in extended-body regime, and the two shear layers separated from the upstream cylinder are kept nearly horizontally and wrap around the downstream cylinder. At intermediate gap ratios (G^*=0.4 and 0.6), however, the lower shear layer is broken into two segments. The one in between the two cylinders deflects upward and reattaches on the leading surface of the downstream cylinder. Similar shear layer deflection and reattachment are evident for L^*=3 at intermediate gap ratios.

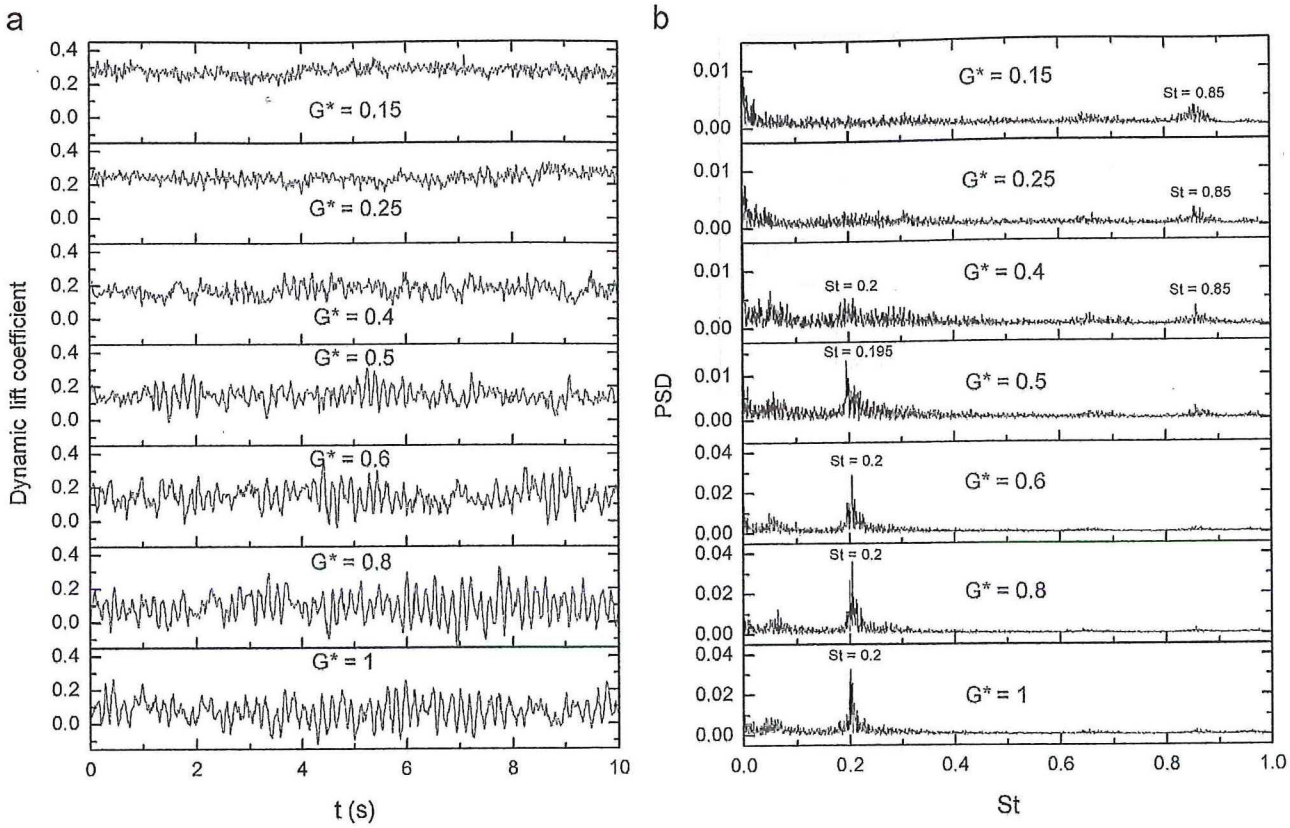

Fig. 5. (a) Time histories of dynamic lift coefficient (C_L) on the near-wall single cylinder at different gap ratios; and (b) corresponding spectra based on power spectral density (PSD) function.

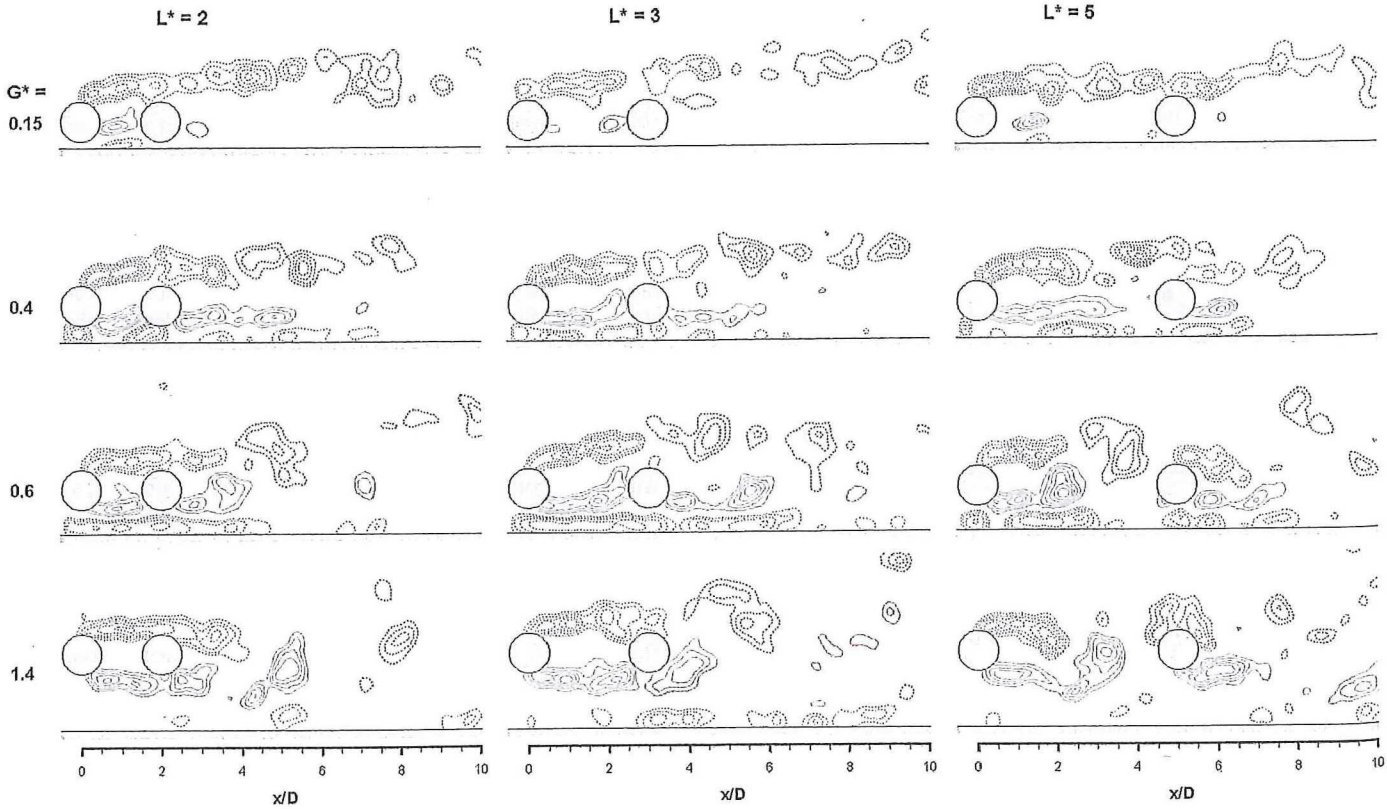

Fig. 6. A representative snapshot of the instantaneous normalized vorticity ($\omega* = \omega D/U$) fields around the near-wall tandem cylinders at L^*=2, 3 and 5 and G^*=0.15, 0.4, 0.6 and 1.4. Positive: solid red lines; negative: dashed blue lines. Cut-off value $|\omega^*|_{min}$=1; contour interval=0.5. (For interpretation of the references to color in this figure, the reader is referred to the web version of this article.)

Based on the PIV measurement results, a map of flow patterns around the near-wall tandem cylinders in the G^*–L^* plane is proposed in Fig. 7. With reference to L^*, it can be roughly divided into three basic types of spacing, that is, close ($1 < L^* < 2$), moderate ($2 < L^* < 4$) and wide ($L^* > 4$), which are roughly equivalent to the 'extended-body', 'reattachment' and 'impinging' regimes, respectively, for free-standing tandem cylinders. Similarly, the flow can be broadly classified as a function of G^*: (i) large-gap regime (approx. > 1), the flow and vortex shedding characteristic are similar to the free-standing case; (ii) intermediate-gap regime (approx. $0.3 < 1$), where periodic vortex shedding occurs, but the strength of vortex shedding reduces with decreasing G^*; and (iii) small-gap regime (approx. $G^* < 0.3$), where periodic vortex shedding is completely suppressed.

3.2.2. *Forces, lift spectra and Strouhal numbers on the downstream cylinder*

This section presents the time histories of fluctuating lift on the downstream cylinder and the corresponding spectra for different

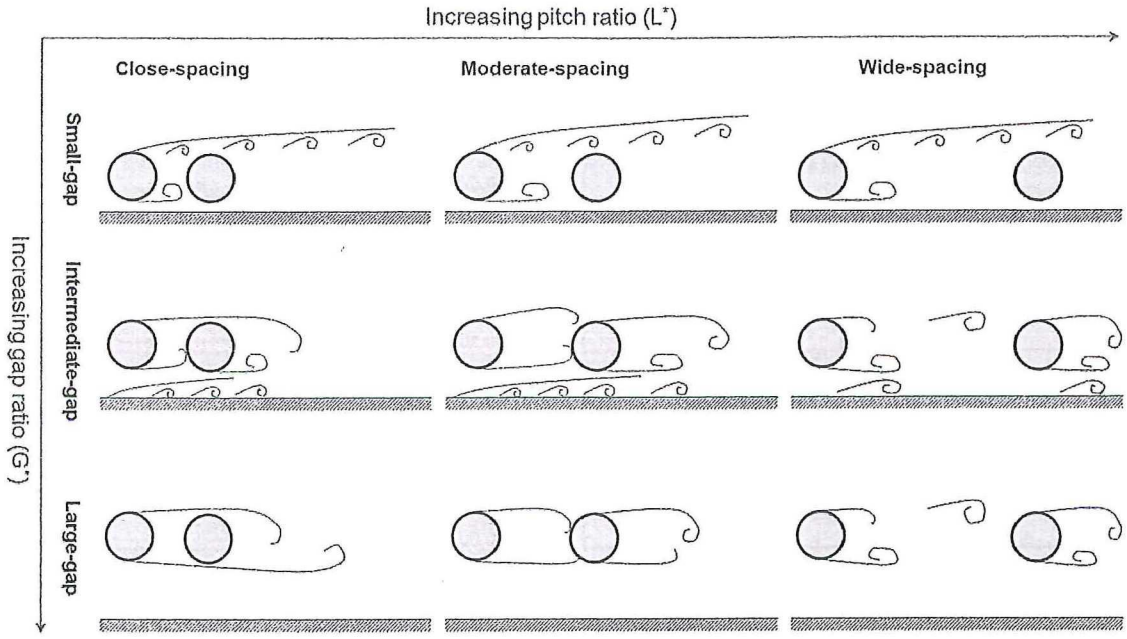

Fig. 7. Overview of flow patterns for the near-wall two tandem cylinders as a function of both G^* and L^*.

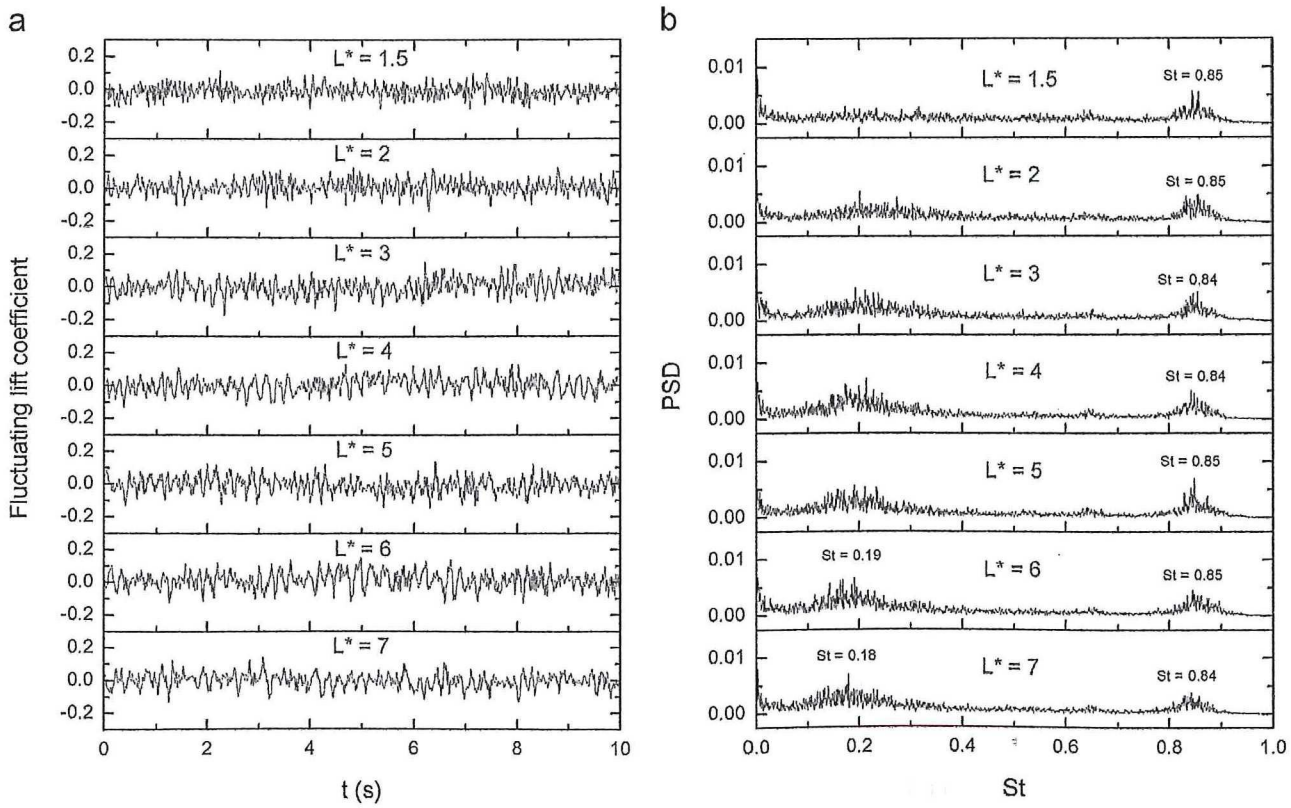

Fig. 8. (a) Time histories of fluctuating lift coefficient; and (b) corresponding spectra on the downstream cylinder for different spacing ratios at G^*=0.15.

combinations to L^* and G^*. The results for $L^*=1.5$–7 at $G^*=0.15$ are shown in Fig. 8. It is clear that the flow is in the vortex-shedding suppression regime. Accordingly, the lift signal is irregular for all spacing ratios considered. Similar to the case of the near-wall single cylinder (Fig. 5), each spectrum displays a peak at $St \approx 0.85$ associated with K-H type of roll-ups. It is noted that for wide-

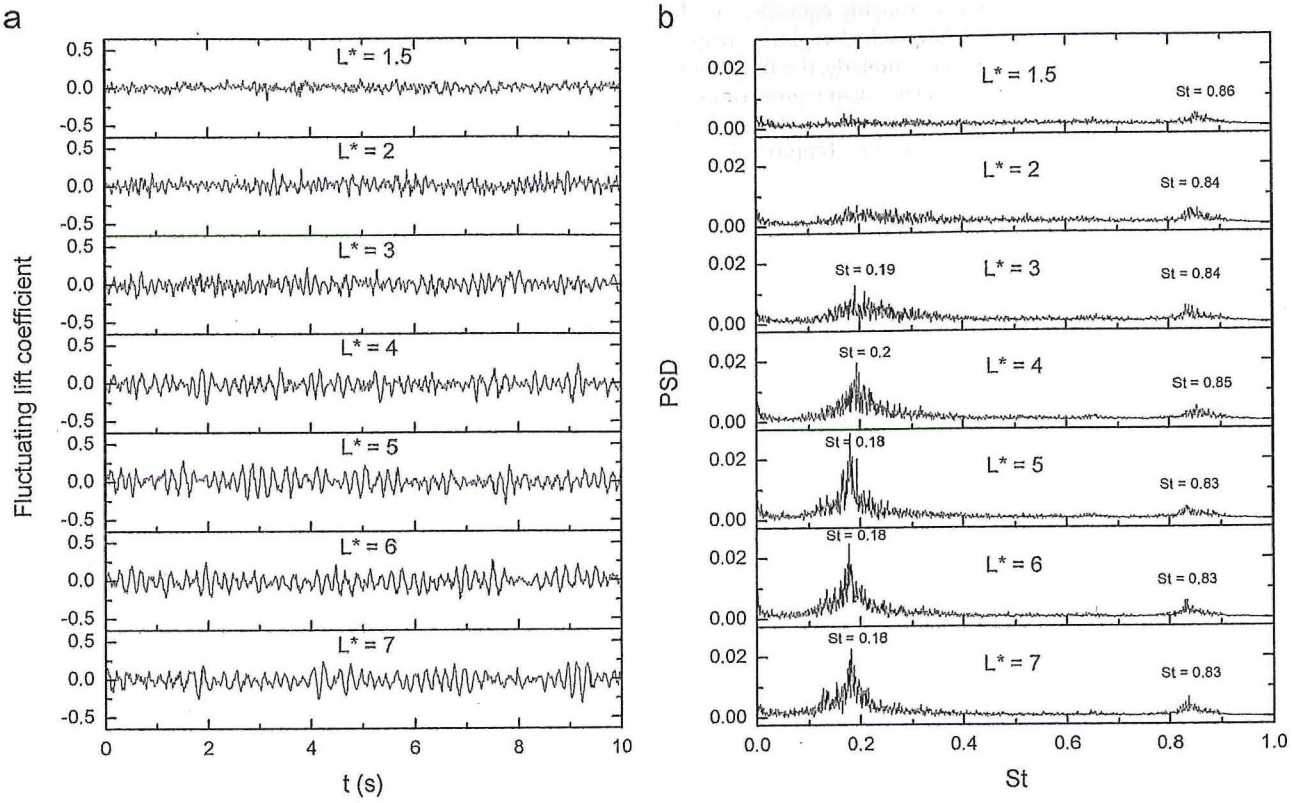

Fig. 9. (a) Time histories of fluctuating lift coefficient; and (b) corresponding spectra on the downstream cylinder for different spacing ratios at $G^*=0.4$.

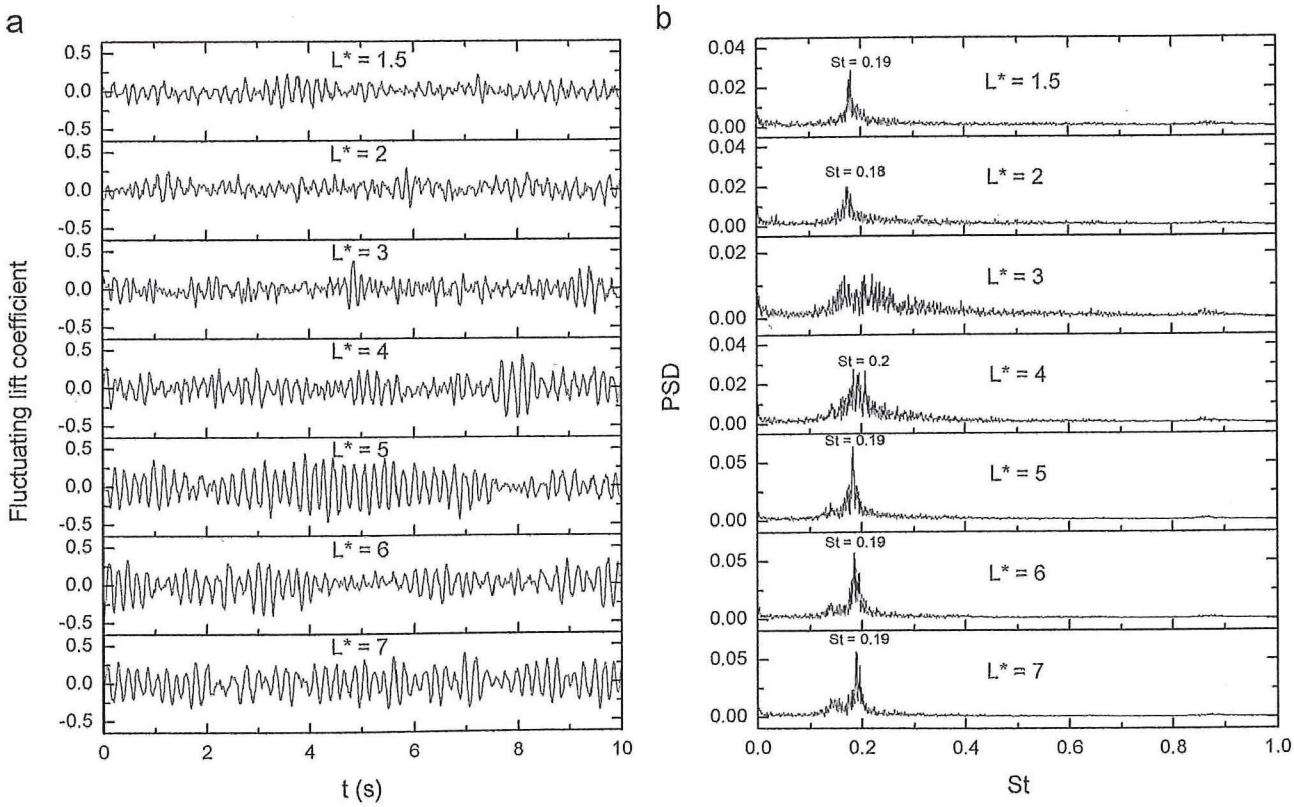

Fig. 10. (a) Time histories of fluctuating lift coefficient; and (b) corresponding spectra on the downstream cylinder for different spacing ratios at $G^*=0.6$.

spacing configuration ($L^* \geq 4$), there is an additional peak around $St \approx 0.18$ (corresponding to the large-scale von Kármán vortex shedding) but it is rather broad-banded.

For $G^*=0.4$ (Fig. 9(a)), the signal gradually changes from a chaotic pattern at $L^*=1.5$ and 2, to a more periodic pattern at $L^* \geq 4$. The amplitude of fluctuation increases sharply with L^* from close- to moderate-L^* ($L^* \leq 4$). As shown in Fig. 9(b), each spectrum always exhibits a peak at $St \approx 0.83$–0.86 associated with the K-H instability, implying that the wall effects are still significant. It should be noted that from $L^*=3$ onward, an additional peak at $St \approx 0.18$ appears as well. The double-peak character indicates the co-existence of two different fluid dynamic processes, as could be appreciated from Fig. 6. Located in the lee of the upstream cylinder, the downstream cylinder is subjected to shear layer reattachment on its surface. At $G^*=0.4$, the shear layers are basically in K-H type of roll-ups. However, when L^* is large enough (e.g., $L^*=5$), discrete 'patches' of vorticity are formed in the wake of the downstream cylinder, indicative of occurrence of vortex shedding at relatively low frequency. Fig. 9(b) shows that in the case of $L^*=3$, the peak at $St \approx 0.19$ is rather broad-banded and small in amplitude; with further increase in L^*, it becomes more distinct, suggesting that vortex shedding becomes more regular and stronger.

The results for $G^*=0.6$ are shown in Fig. 10. In this case, the lift signal becomes significantly more periodic than that of $G^*=0.4$ at the same spacing ratio. On the other hand, the peak for the high-frequency K-H roll-ups becomes nearly invisible as a tiny hump, indicating that the wall effects reduce with increasing G^*. All the spectra except for those at $L^*=3$ and 4 display a dominant frequency of $St=0.18$–0.2 corresponding to periodic vortex shedding. At $L^*=3$ and 4, however, the spectral peak is rather broad-banded, suggestive of weakened vortex shedding activity.

At $G^* > 1$, the wall effects become nearly negligible, see Fig. 11 for $G^*=1.4$. The high-frequency component that may otherwise exist at small- and intermediate-G^* disappears completely, so each spectrum is characterized by a well-defined frequency at $St=0.15$–0.19. Based on the proposed classification, they belong to extended-body regime ($L^*=1.5$ and 2), reattachment regime ($L^*=3$ and 4), and impinging regime ($L^*=5$, 6 and 7), respectively. Several features can be observed. Firstly, in either extended-body or impinging regime, the peak is well-defined, while in reattachment regime ($L^*=3$ and 4) it is somewhat broad-banded. Secondly, the periodicity of lift signal does not vary monotonically with L^*; instead, it first achieves a minimum at $L^*=3$ (onset of reattachment regime) and then a maximum at $L^*=5$ (onset of impinging

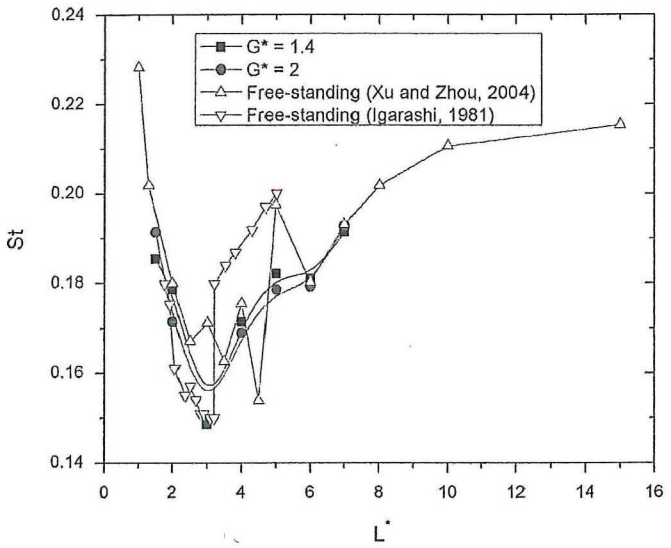

Fig. 12. Variation of Strouhal number (St) with L^* at large gap ratios, together with published data on two tandem cylinders under free-standing conditions.

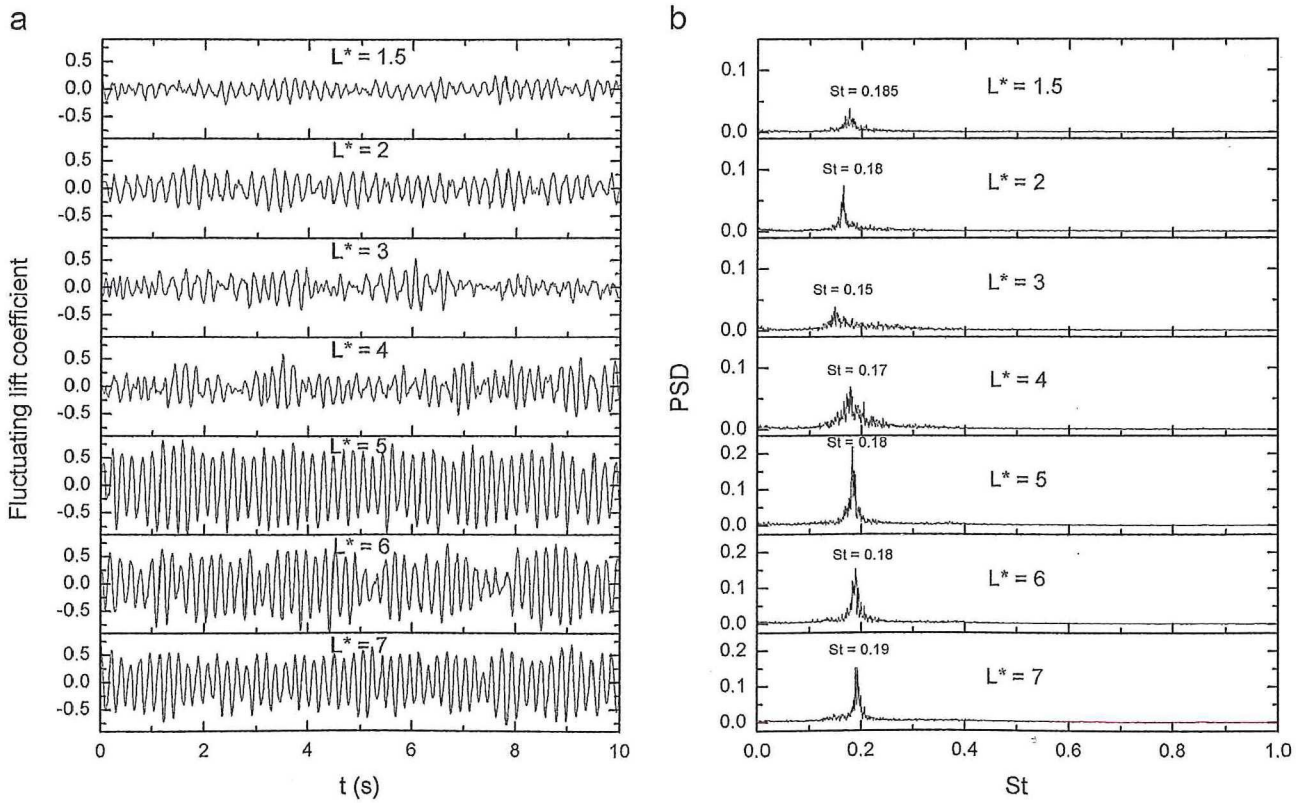

Fig. 11. (a) Time histories of fluctuating lift coefficient; and (b) corresponding spectra on the downstream cylinder for different spacing ratios at $G^*=1.4$.

regime), as indicated by the amplitude of lift fluctuation or the magnitude of spectral peak. These observations indicate that the downstream cylinder is influenced by the advection and impingement of vortices shed from the upstream cylinder. At $L^* \geq 5$, the peak continues to decrease in magnitude with increasing L^*, suggesting that the interference between the two cylinders is reducing.

Fig. 11(b) shows that the values of St for the spectral peak in impinging regime ($L^* \geq 5$) maintain approximately constant. For $L^* \leq 4$, on the other hand, St first drops with L^* from 0.185 at $L^*=1.5$ to a minimum of 0.15 at $L^*=3$, and then recovers to 0.17 at $L^*=4$. The initial decline of St with L^* at small- to moderate-L^* seems to be an inherent feature when the wall proximity effects are negligible, since a similar trend is found for $G^*=2$ as well as for free-standing tandem cylinders published in the literature (e.g., Igarashi 1981; Xu and Zhou, 2004), as shown in Fig. 12. This is likely attributed to the fact that an increase in L^* allows the shear layers emanated from the upstream cylinder to grow thicker upon reaching the surface of the downstream cylinder. Accordingly, St decreases progressively with L^*, because a thicker shear layer leads to a lower vortex shedding frequency from a cylinder (Roshko, 1954). However, this trend cannot be sustained with further increase in L^* since the flow would change into impinging regime at $L^*_{cr} \approx 4$, for which the shear layers emanated from the upstream cylinder will roll up into discrete vortices in between the two cylinders and are no longer directly connected with the vortex formation from the downstream cylinder.

The force data indicate that the wall proximity tends to inhibit periodic vortex shedding from the cylinders. Furthermore, spectral analysis was applied to the velocity data to illustrate the periodic

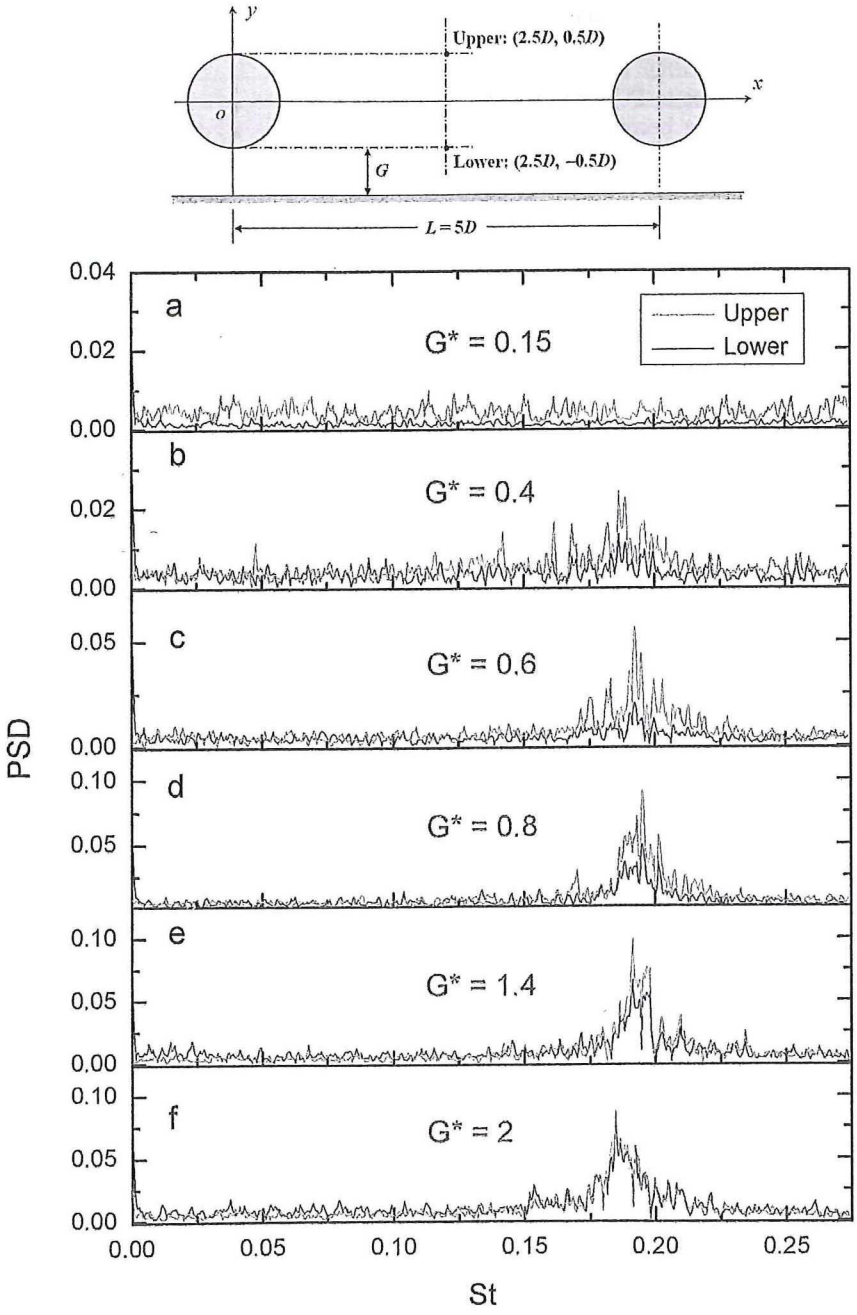

Fig. 13. Spectra of transverse velocity (v) in between the two cylinders for the case of $L^*=5$ at: (a) $G^*=0.15$, (b) 0.4, (c) 0.6, (d) 0.8, (e) 1.4 and (f) 2. The velocity signals are retrieved from: $(x,y)=(2.5D, -0.5D)$, i.e., in the lower shear layer; and $(x,y)=(2.5D, 0.5D)$, i.e., in the upper shear layer.

nature of the flow up to $f=7.5$ Hz (i.e., half the PIV sampling rate of 15 Hz), or St ≈ 0.27. Fig. 13 shows the velocity spectra between the two cylinders for the case of $L^*=5$ at different gap ratios. The velocity signals are retrieved from $(x,y)=(2.5D, -0.5D)$ and $(2.5D, -0.5D)$, which are respectively located in the lower and upper shear layers. At $G^*=0.15$, there is no peak over the measurement range, whereas at $G^* \geq 0.4$, each spectrum begins to exhibit a dominant peak at St=0.17–0.2 (which is in accordance with the low-frequency component in lift spectra). This confirms the validity of using lift signal as an indicator of vortex shedding process. The peak magnitude increases with G^* particularly over the range of $G^* \leq 0.8$, suggesting that the effects of wall proximity are decreasing and the strength of vortex shedding becomes stronger (similar conclusion is inferred from the lift spectra). It is noteworthy that for a given G^*, the peak in the upper shear layer (denoted by red line) is generally higher in magnitude than that in the lower shear layer (denoted by black line) for $G^* \leq 1.4$, indicating flow asymmetry about the wake centerline. At large enou gh gap ratios (e.g., $G^*=2$), the two spectra almost coincide with each other.

Fig. 14 presents the variations of the mean drag ($\overline{C}_D$) and lift ($\overline{C}_L$), RMS drag (C_D') and lift (C_L') coefficients on the downstream cylinder as a function of L^* for different gap ratios, together with the corresponding values of the isolated single cylinder for comparison. Located in the lee of the upstream cylinder, the mean drag coefficient on the downstream cylinder ($\overline{C}_D$) remains consistently lower than that of the isolated cylinder. As shown in Fig. 14(a), $\overline{C}_D$ increases monotonically with L^* for all gap ratios considered, but

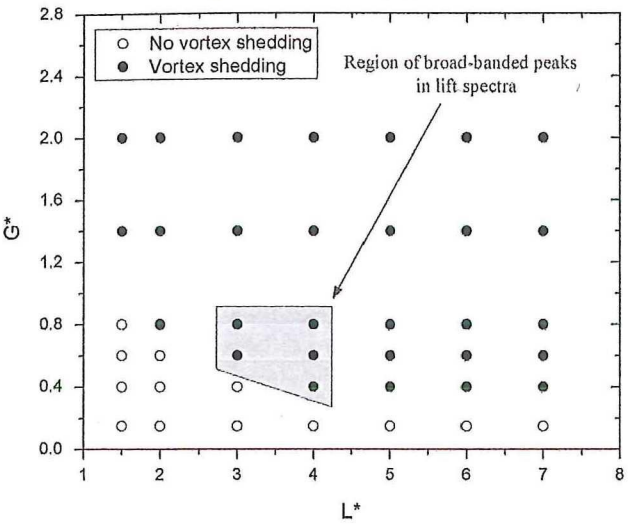

Fig. 15. Critical gap and spacing ratios (G^*_{cr} and L^*_{cr}) for onset of vortex shedding from the downstream cylinder.

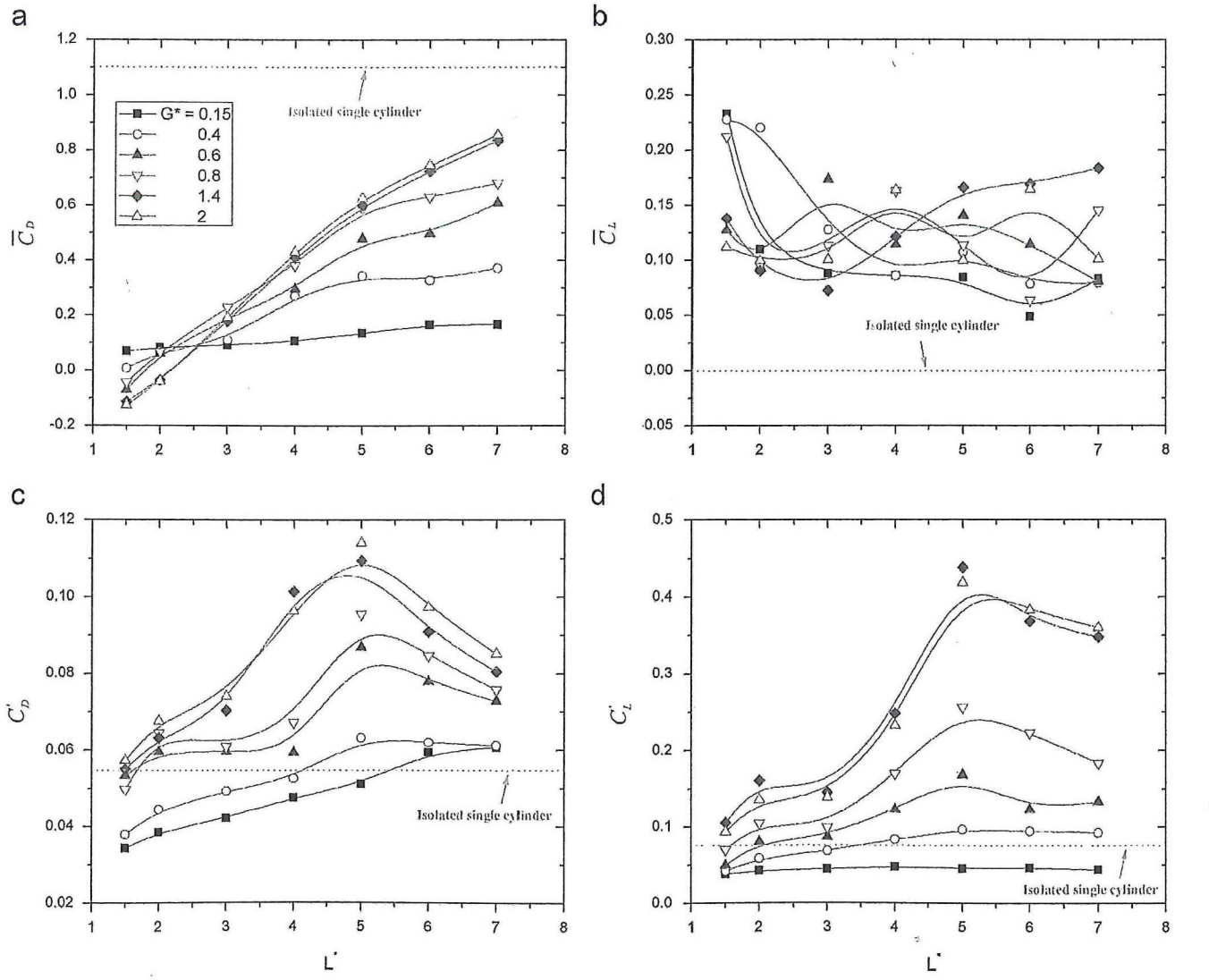

Fig. 14. Variation of dynamic force coefficients on the downstream cylinder with L^* at different gap ratios: (a) mean drag coefficient ($\overline{C}_D$); (b) mean lift coefficient ($\overline{C}_L$); (c) RMS drag coefficient (C_D'); and (d) RMS lift coefficient (C_L').

at different rates (as reflected by slope of the curves). At $G^*=0.15$, $\overline{C}_D$ is about 0.1 and increases slightly with L^*. As G^* increases to 2, the low end of each curve (at $L^*=1.5$) decreases until reaching a minimum of $(\overline{C}_D)_{\min}=-0.13$, whereas the high end (at $L^*=7$) continues to rise up to $(\overline{C}_D)_{\max}=0.84$. Therefore, when G^* is relatively large ($G^*\geq 0.8$), the downstream cylinder experiences a drag inverse (from negative to positive) within the range of $2\leq L^*\leq 3$. This is a well-known phenomenon for free-standing tandem cylinders, for instance, Sumner et al. (2005) reported a minimum of $(\overline{C}_D)_{\min}=-0.55$ at $L^*=1.125$. The negative (attractive) drag at small-L^* is due to the fact that the downstream cylinder is completely enwrapped by the shear layers from the upstream cylinder, and hence experiences a negative pressure. The mean lift coefficient ($\overline{C}_L$), as shown in Fig. 14(b), on the other hand, varies significantly with both G^* and L^*. Similar to the near-wall single cylinder, the downstream cylinder generally experiences a positive

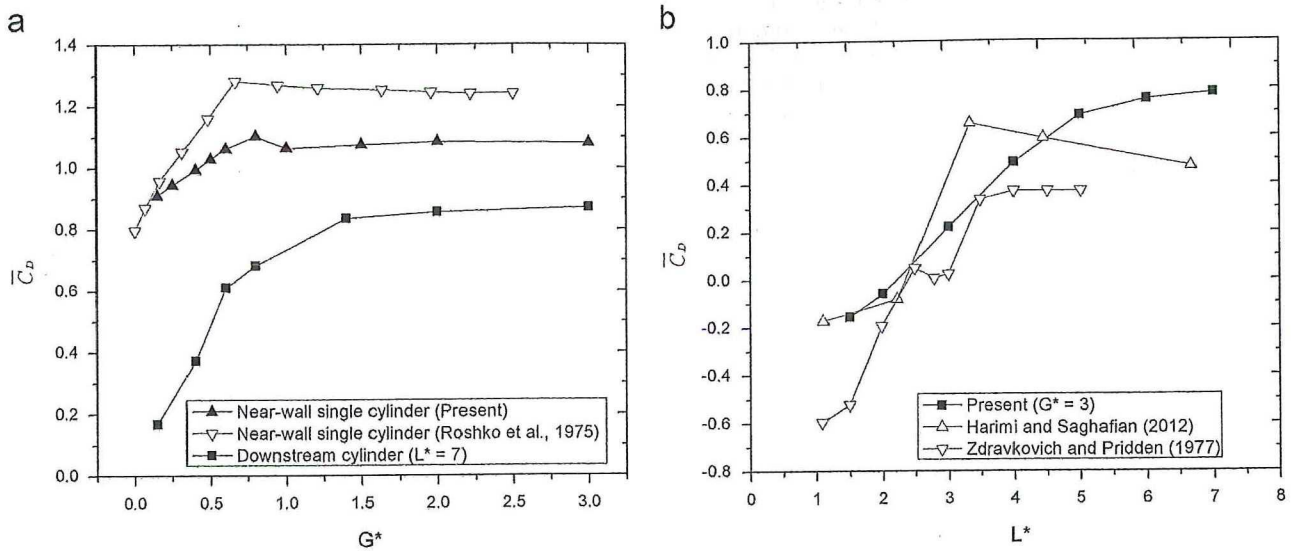

Fig. 16. Variation of the mean drag coefficient ($\overline{C}_D$) on the downstream cylinder with: (a) G^* at large spacing ratio ($L^*=7$), and comparison with published data (Roshko et al., 1975) and the present measurement data on a near-wall single cylinder; and (b) L^* at large spacing ratio ($G^*=3$), and comparison with published data under free-standing conditions (Zdravkovich and Pridden, 1977; Harimi and Saghafian, 2012).

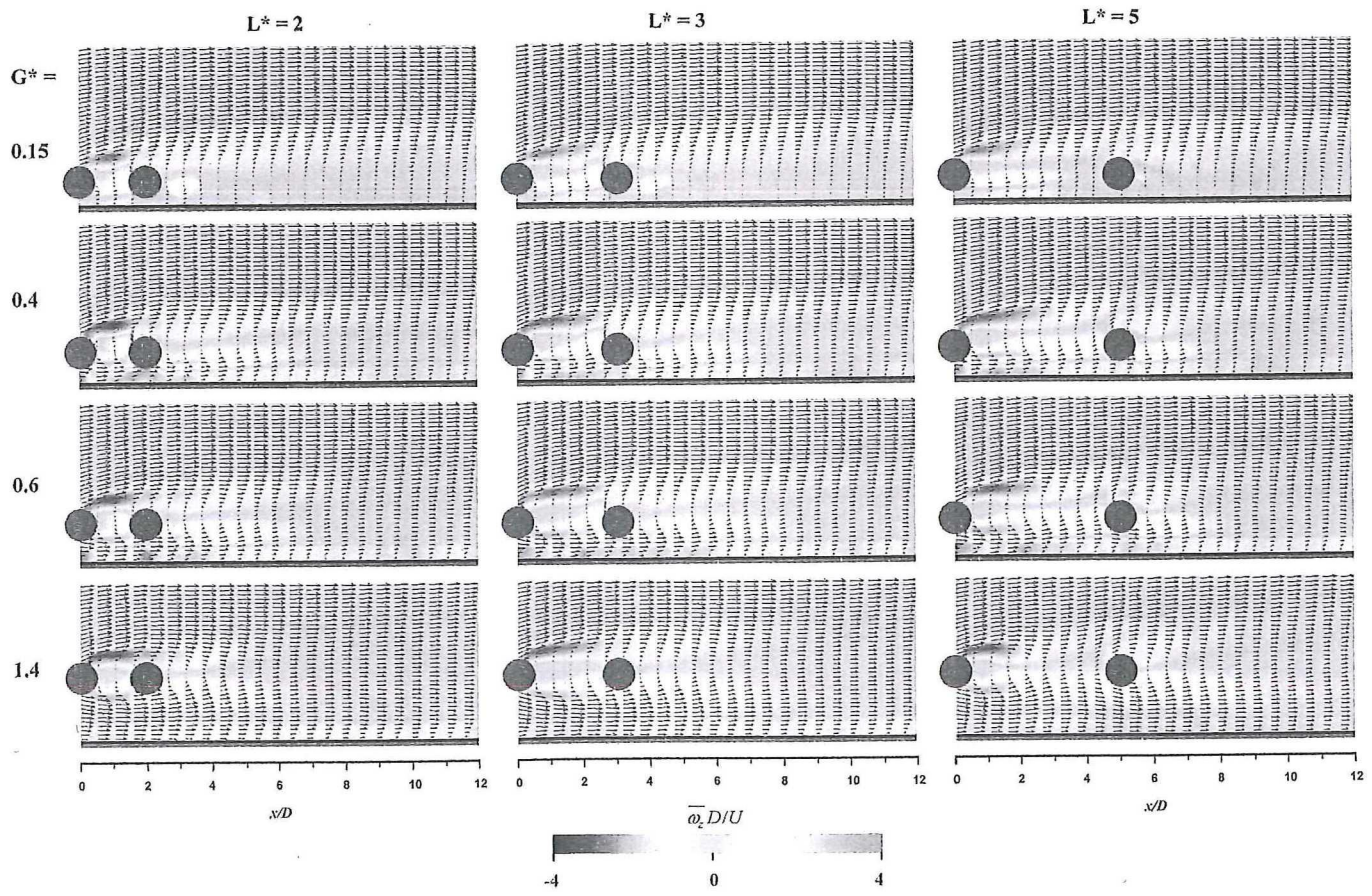

Fig. 17. Mean velocity vector fields for $L^*=2$, 3 and 5 and $G^*=0.15$, 0.4, 0.6 and 1.4. Superimposed with contours of the normalized spanwise mean vorticity ($\overline{\omega}_z D/U$).

mean lift ($\overline{C}_L > 0$), but it is considerably smaller in amplitude ($\overline{C}_L \approx 0.05$–$0.2$). The significant variation of $\overline{C}_L$ with G^* and L^* is probably due to the following two reasons. The first is the possible misalignment of the models, since it is extremely difficult, if not impossible, to achieve a perfect alignment experimentally. Secondly, the flow in the gap may keep steadily reattached on the surface of the downstream cylinder, but may also spontaneously flip-flop vertically so that the reattachment point varies irregularly over time, which is in analogy to the flow between two side-by-side cylinders at small gap ratios (Sumner et al., 1999). Figs. 14 (c) and 14(d) show that the variation trends of C_D' and C_L' with L^* are similar, although the latter has a much higher (3∼4 times) magnitude. In general, C_D' and C_L' display different variation trends with respect to L^* depending on the value of G^*, which is consistent with the PIV data. At $G^*=0.15$ when vortex shedding is suppressed, C_D' and C_L' increase steadily with L^* over the measurement range. In intermediate-gap regime ($G^*=0.4$, 0.6 and 0.8), they increase rapidly with L^* until reaching a maximum at $L^*=5$ (i.e., onset of impinging regime). A similar convex shape is found for $G^*=1.4$ and 2, where the two curves almost coincide, implying diminishing effects of wall proximity.

Depending on the values of G^* and L^*, the shear layers emanated from the upstream cylinder may overshoot, reattach or impinge upon the downstream cylinder and then separate, perhaps joining those developed on the downstream cylinder itself, to form vortices around the downstream cylinder. This results in different behaviors of fluid dynamic forces on the downstream cylinder. Here, an attempt is made to identify the critical gap (G^*_{cr}) and spacing (L^*_{cr}) ratios for vortex shedding based on the periodicity of fluctuating lift signals and the intensity of the peak in lift spectra as shown in Figs. 8 – 11 (similar observation can be obtained by analysis of the velocity signal as shown in Fig. 13). The map for absence/presence of vortex shedding from the downstream cylinder in G^*–L^* plane is presented in Fig. 15. The vortex-shedding suppression regime is mainly located at the lower-left corner (i.e., small-G^* and small-L^*): at the smallest gap ratio ($G^*=0.15$), it extends the whole L^* range; as G^* increases, it gradually shrinks in width until completely disappears at $G^*=0.8$. In addition, the values of C_L' can be used to

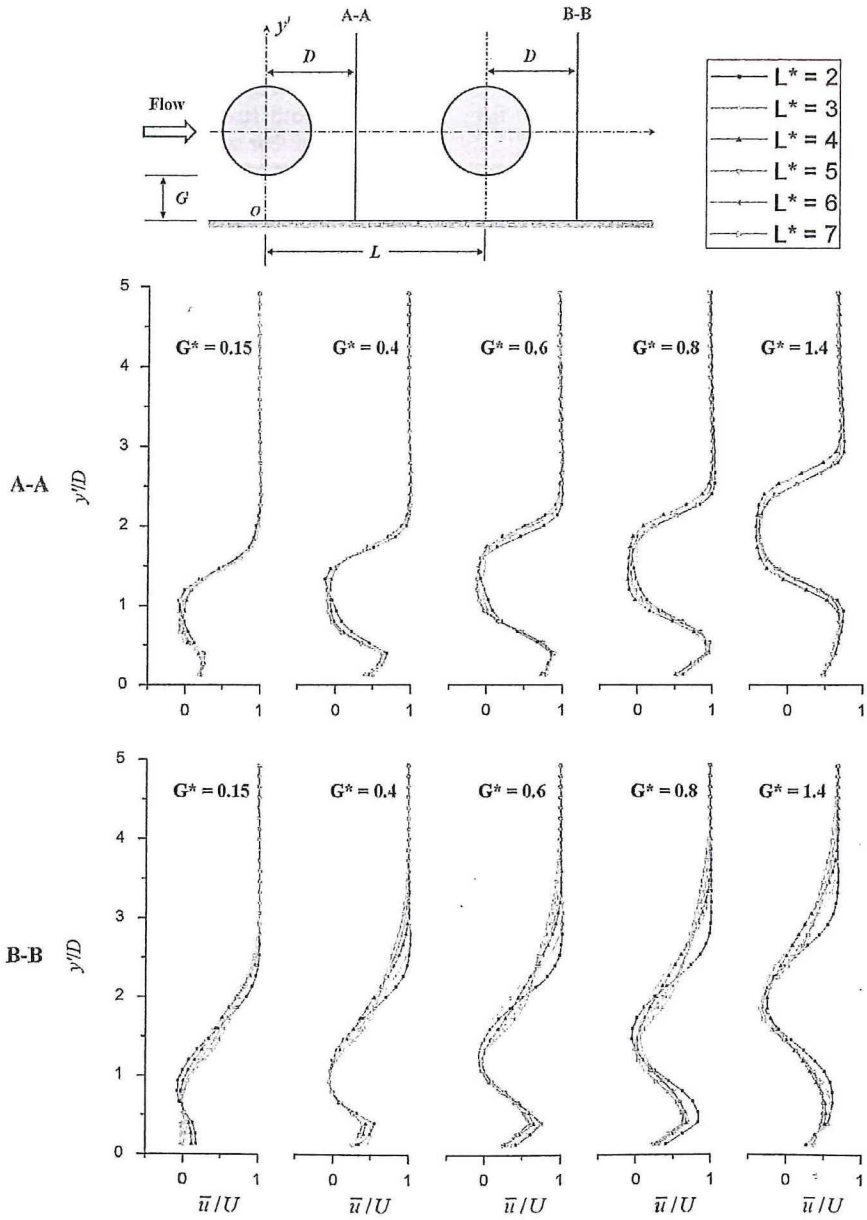

Fig. 18. Profiles of the normalized streamwise mean velocity ($\overline{u}/U$) along two vertical lines (i.e., A-A and B-B, located behind the upstream cylinder and the downstream cylinder, respectively) for different gap and spacing ratios.

qualitatively determine the strength of vortex shedding. It should be noted that measurements with a higher resolution in G^*–L^* plane are desirable in order to more accurately define the boundaries separating the different flow regimes. Furthermore, as shown in Figs. 9 – 11, due to enhanced activity of shear layer reattachment for $L^*=3$ and 4 in intermediate-G^* regime, the spectral peak is broad-banded in these cases, which has been highlighted by the shaded region in Fig. 15.

As shown in Fig. 16(a), variations of the mean drag coefficient ($\overline{C}_D$) on the downstream cylinder with G^* at the largest spacing ratio ($L^*=7$) have been compared with the published data (Roshko et al., 1975) and the present measurement on a near-wall single cylinder. Similar to the case of the single cylinder, $\overline{C}_D$ initially experiences a sharp increase with G^* before leveling off at large enough gap ratios ($G^* \geq 1$). However, at the same G^* it is appreciably lower than that of the single cylinder (particular when G^* is small), due to the effects from the upstream cylinder. This suggests that the spacing ratio of $L^*=7$ is still not sufficiently large for the two tandem cylinders to be considered independently. On the other hand, as shown in Fig. 16(b), the variation of $\overline{C}_D$ with L^* at $G^*=3$ agrees well with the published data under free-standing conditions (Zdravkovich and Pridden, 1977; Harimi and Saghafian, 2012), confirming that the gap ratio of $G^*=3$ is large enough for neglecting the wall effects.

3.2.3. *Ensemble-averaged flow patterns around the cylinders*

As shown above, the vortex shedding characteristics from the cylinders depend on both G^* and L^*. This leads to corresponding variation in the statistical quantities of the flow, such as distributions of mean velocity vectors and Reynolds shear stresses.

Consistent with the instantaneous flow structure, the mean velocity vector field (Fig. 17) gradually changes from asymmetrical patterns about the wake centerline at small- and intermediate-gap ratios ($G^* < 1$), to symmetrical patterns at large gap ratios ($G^* > 1$). For a given L^*, the recirculation length, defined as the distance from the cylinder base to the zero mean streamwise velocity point along the wake centerline, increases with G^*. Meanwhile, the gap flow is deflected upward in y-direction and reattach on the leading face of the downstream cylinder, most notably in the case of intermediate-G^* and moderate-L^* (e.g., $G^*=0.6$ and $L^*=3$). This corresponds to the region of broad-banded peaks in the lift spectra, as shown in Fig. 15.

Profiles of the normalized streamwise mean velocity ($\overline{u}/U$) along two vertical lines located at $0.5D$ after the trailing edges of the two cylinders (i.e., A-A and B-B) for different gap and spacing ratios are provided in Fig. 18. One obvious feature is that for a fixed G^*, the profiles at different L^* at A-A almost collapse, whereas those at B-B deviate from each other more evidently. This indicates that the presence of the downstream cylinder mainly affects the flow behind it. The presence of the cylinders results in the velocity defect behind each cylinder, so that the velocity profiles exhibit as an "S"-shape. When $G^* < G^*_{cr}$ (e.g., $G^*=0.15$), however, the lower half of the "S"-shape is not obvious or even completely disappears due to the rather weak gap flow.

Furthermore, the shear layer developments can be appreciated from the contours of the normalized Reynolds shear stress ($\overline{u'v'}/U^2$) in Fig. 19. At small- or intermediate-G^*, the upper shear layer is both stronger in magnitude and larger in size than the lower one. For a given L^*, as G^* increases from 0.15 to 1.4, the distributions of $\overline{u'v'}/U^2$ gradually become more symmetric about the wake centerline; meanwhile, regions of significant $\overline{u'v'}/U^2$ contract in the streamwise direction (to smaller x), together with elevated level (or magnitude) of $\overline{u'v'}/U^2$.

Similar to the flow classification based on the instantaneous vorticity fields, the distributions of $\overline{u'v'}/U^2$ can be divided into three different patterns – Pattern 1: regions of significant $\overline{u'v'}/U^2$ are found in the wake of the downstream cylinder only (e.g., for all

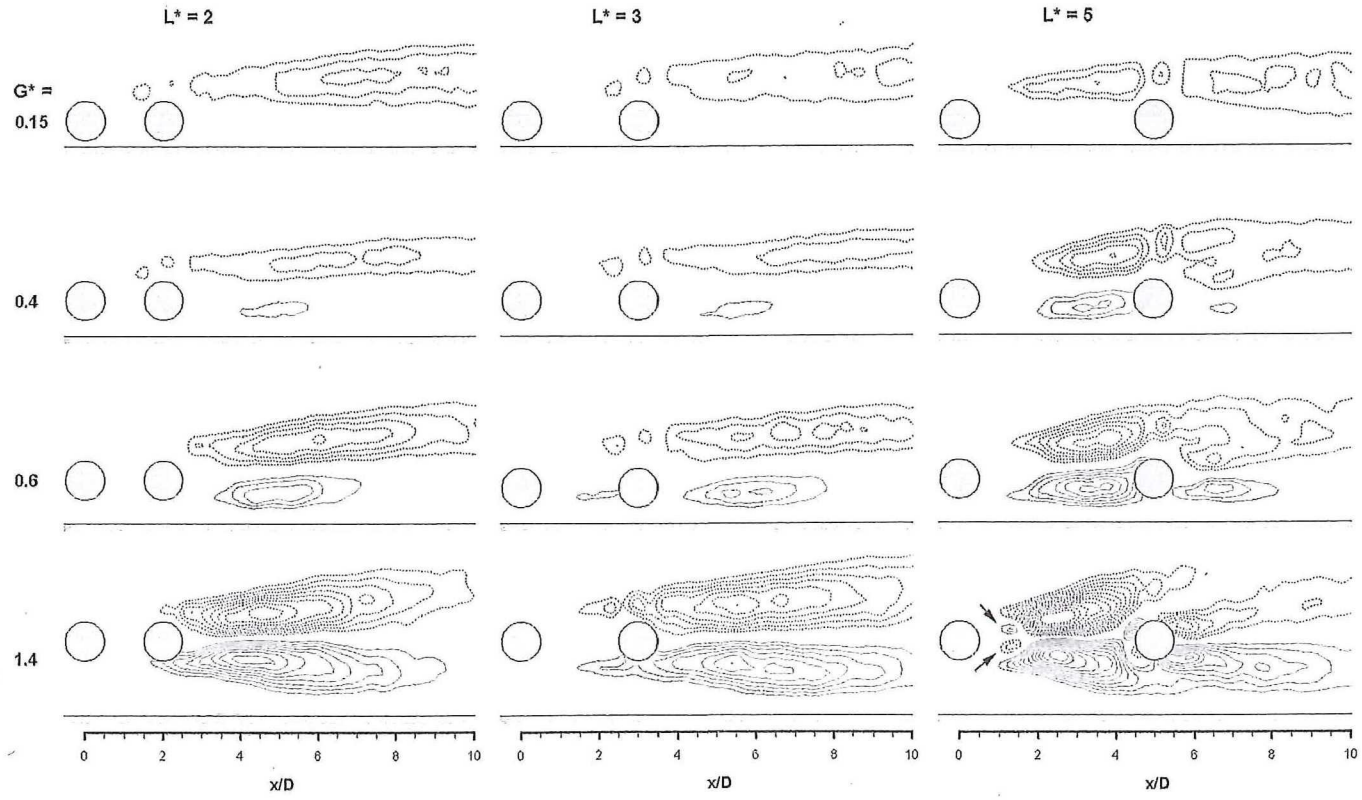

Fig. 19. Contours of the normalized Reynolds shear stress ($\overline{u'v'}/U^2$) for $L^*=2$, 3 and 5 and $G^*=0.15$, 0.4, 0.6 and 1.4. Positive: solid red lines; negative: dashed blue lines. Cut-off value $\left|\overline{u'v'}/U^2\right|_{min}=0.01$; contour interval=0.005 (For interpretation of the references to color in this figure, the reader is referred to the web version of this article.).

gap ratios at $L^*=2$, and for relatively small gap ratios $G^* \leq 0.6$ at $L^*=3$); Pattern 2: only the upper shear layer is evident, which is, however, located not only behind the downstream cylinder, but also in the space between the two cylinders (e.g., for $G^*=0.15$ and $L^*=5$); Pattern 3: both the lower and upper shear layers are observable in between the two cylinders (e.g., for $G^* \geq 0.4$ and $L^*=5$, and for $G^*=1.4$ and $L^*=3$).

The distributions of $\overline{u'v'}/U^2$ for the case of $G^*=1.4$ and $L^*=5$ (where the wall effects are negligible and the flow is in impinging regime) are noteworthy. In the wake of the upstream cylinder, besides the two large-scale clusters of $\overline{u'v'}/U^2$, there are two additional small-scale clusters of opposite-signed vorticity immediately located upstream of the main shear layers (as highlighted by black arrows). This feature agrees with the results of Dong et al. (2006) on an isolated single cylinder at Re=4000 and 10 000. The distributions of $\overline{u'v'}/U^2$ in the wake of the downstream cylinder are confined to a smaller region as compared to those of the upstream cylinder.

4. Concluding remarks

Flow around two near-wall tandem cylinders at Re=6300 has been investigated extensively for 6 gap ratios (G^*=0.15, 0.4, 0.6, 0.8, 1.4 and 2) and 7 inter-cylinder spacing ratios (L^*=1.5, 2, 3, 4, 5, 6 and 7), making 42 combinations in total. The results show that both the flow patterns (instantaneous and ensemble-average) and the dynamic forces (drag and lift) are highly dependent on the combined values of G^* and L^*, due to mixed effects of wall proximity and mutual interference between the two cylinders.

With reference to L^*, the flow interference between the two cylinders changes from extended-body regime at close-spacing ratios ($1<L^*<2$), reattachment regime at moderate-spacing ratios ($2<L^*<4$), to impinging regime at wide-spacing ratios ($L^*>4$). However, this classification is valid only for large gap ratios ($G^*>1$).

The nearby wall tends to promote the K-H type of roll-ups and inhibit periodic vortex shedding from the cylinders. Therefore, in intermediate-gap regime ($0.3<G^*<1$) vortex shedding takes places but in an asymmetric manner about the wake centerline, whereas in small-gap regime ($G^*<0.3$) vortex shedding is suppressed completely. When $G^* \leq 0.4$, the lift spectrum displays a double-peak mode for $L^* \geq 3$, namely, St ≈ 0.18–0.2 and 0.83–0.85, indicating the co-existence of two instability mechanisms (i.e., von Kármán vortex shedding and K-H roll-up). On the other hand, either an increment or a decrement in G^* would result in single-peak mode, that is, St ≈ 0.84 for G^*=0.15, and St ≈ 0.19 for $G^* \geq 0.6$.

For close- and moderate-spacing configurations, the shear layers emanated from the upstream cylinder (which would otherwise be kept roughly horizontal) deflect upwards and reattach on the leading surface of the downstream cylinder, leads to relatively higher mean drag ($\overline{C}_D$) and RMS drag/lift (C_D' and C_L') coefficients on the latter. The enhanced activity of shear layer reattachment also results in broadened spectral peak for vortex shedding at moderate-L^* (L^*=3–4) and intermediate-G^* (G^*=0.4–0.8). The study also attempts to quantitatively identify the critical gap (G^*_{cr}) and spacing (L^*_{cr}) ratios for the onset of vortex shedding from the downstream cylinder based on the fluctuating lift and the lift spectra.

Acknowledgments

Funding support from Singapore National Research Foundation (NRF) through the Competitive Research Programme (CRP) under Grant no. NRF-CRP5-2009-01 is acknowledged. Hao Z. wishes to acknowledge the support from Shanghai Municipal Education Commission Project (No. 12ZZ149) and Science and Technology Commission of Shanghai Municipality (No. 10PJ1404700).

References

Bearman, P.W., Zdravkovich, M.M., 1978. Flow around a circular cylinder near a plane boundary. J. Fluid Mech. 89, 33–47.
Bhattacharyya, S., Dhinakaran, S., 2008. Vortex shedding in shear flow past tandem square cylinders in the vicinity of a plane wall. J. Fluids Struct 24, 400–417.
Buresti, G., Lanciotti, A., 1992. Mean and fluctuating forces on a circular cylinder in cross-flow near a plane surface. J. Wind Eng. Ind. Aerodyn. 41, 639–650.
Carmo, B.S., Meneghini, J.R., Sherwin, S.J., 2010. Possible states in the flow around two circular cylinders in tandem with separations in the vicinity of the drag inversion spacing. Phy. Fluids 22, 003005PHF.
Dipankar, A., Sengupta, T.K., 2005. Flow past a circular cylinder in the vicinity of a plane wall. J. Fluids Struct 20, 403–423.
Dong, S., Karniadakis, G.E., Ekmekci, A., Rockwell, D., 2006. A combined direct numerical simulation-particle image velocimetry study of the turbulent near wake. J. Fluid Mech. 569, 185–207.
Fouras, A., Soria, J., 1998. Accuracy of out-of-plane vorticity measurement derived from in-plane velcotiy field data. Exp. Fluids 25, 409–430.
Gerrard, J.H., 1967. Experimental investigation of separated boundary layer undergoing transition to turbulence. Phy. Fluids 10, S98–S100.
Harichandan, A.B., Roy, A., 2012. Numerical investigation of flow past single and tandem cylindrical bodies in the vicinity of a plane wall. J. Fluids Struct 33, 19–43.
Harimi, I., Saghafian, M., 2012. Numerical simulation of fluid flow and forced convection heat transfer from tandem circular cylinders using overset grid method. J. Fluids Struct 28, 309–327.
Huerre, P., Monkewitz, P.A., 1990. Local and global instabilities in spatially developing flows. Annu. Rev. Fluid Mech. 22, 473–537.
Igarashi, T., 1981. Characteristics of the flow around two circular cylinders arranged in tandem – 1. B. JSME 24, 323–331.
Lam, K., Zou, L., 2010. Three-dimensional numerical simulations of cross-flow around four cylinders in an in-line square configuration. J. Fluids Struct 26, 482–502.
Lee, K., Yang, K.-S., Yoon, D.-H., 2009. Flow-induced forces on two circular cylinders in proximity. Comput. Fluids 38, 111–120.
Lei, C., Cheng, L., Kavanagh, K., 1999. Re-examination of the effect of a plane boundary on force and vortex shedding of a circular cylinder. J. Wind Eng. Ind. Aerodyn. 80, 263–286.
Lin, W.-J., Lin, C., Hsieh, S.-C., Dey, S., 2009. Flow characteristics around a circular cylinder placed horizontally above a plane boundary. J. Eng. Mech. 135, 697–716.
Ljungkrona, L., Norberg, Ch., Sundén, B., 1991. Free-stream turbulence and tube spacing effects on surface pressure fluctuations for two tubes in an in-line arrangement. J. Fluids Struct 5, 701–727.
Mahir, N., 2009. Three-dimensional flow around a square cylinder near a wall. Ocean Eng. 36, 357–367.
Maiti, D.K., 2012. Numerical study on aerodynamic characteristics of rectangular cylinders near a wall. Ocean Eng. 54, 251–260.
Maiti, D.K., Bhatt, R., 2014. Vortex shedding suppression and aerodynamic characteristics of square cylinder due to offsetting of rectangular cylinders towards a plane. Ocean Eng. 82, 91–104.
Nishino, T., Roberts, G.T., Zhang, X., 2007. Vortex shedding from a circular cylinder near a moving ground. Phy. Fluids 19, 025103.
Norberg, C., 2003. Fluctuating lift on a circular cylinder: review and new measurements. J. Fluids Struct 17, 57–96.
Ong, M.C., Holmedal, L.E., Myrhaug, D., 2012. Numerical simulation of suspended particles around a circular cylinder close to a plane wall in the upper-transition flow regime. Coast. Eng. 61, 1–7.
Price, S.J., Sumner, D., Smith, J.G., Leong, K., Païdoussis, M.P., 2002. Flow visualization around a circular cylinder near to a plane wall. J. Fluids Struct 16, 175–191.
Rajagopalan, S., Antonia, R.A., 2005. Flow around a circular cylinder-structure of the near wake shear layer. Exp. Fluids 38, 393–402.
Roshko, A., 1954. On the drag and shedding frequency of two-dimensional bluff bodies. NACA Technical Note No, 3169.
Roshko, A., Steinolfson, A., Chattoorgoon, V., 1975. Flow forces on a cylinder near a wall or near another cylinder. Proceedings of the Second U.S. National Conference on Wind Engineering Research, in Colorado State University, Fort Collins, IV-15.
Sakamoto, H., Haniu, H., Obata, Y., 1987. Fluctuating forces acting on two square prisms in a tandem arrangement. J. Wind Eng. Ind. Aerodyn. 26, 85–103.
Sarkar, S., Sarkar, S., 2010. Vortex dynamics of a cylinder wake in proximity to a wall. J. Fluids Struct 26, 19–40.
Sumner, D., 2010. Two circular cylinders in cross-flow: a review. J. Fluids Struct 26, 849–899.
Sumner, D., Richards, M.D., Akosile, O.O., 2005. Two staggered circular cylinders of equal diameter in cross-flow. J. Fluids Struct 20, 255–276.
Sumner, D., Wong, S.S.T., Price, S.J., Païdoussis, M.P., 1999. Fluid behavior of side-by-side circular cylinders normal to a stream. J. Fluids Struct 13, 309–338.

Tadrist, H., Martin, R., Tadrist, L., Seguin, P., 1990. Experimental investigation of fluctuating forces exerted on a cylindrical tube (Reynolds numbers from 3000 to 30 000). Phys. Fluids A 2, 2176–2182.
Wang, X.K., Hao, Z., Tan, S.K., 2013. Vortex-induced vibrations of a neutrally buoyant cylinder near a plane wall. J. Fluids Struct 39, 188–204.
Wang, X.K., Tan, S.K., 2008a. Near-wake flow characteristics of circular cylinder close to a wall. J. Fluids Struct 24, 605–627.
Wang, X.K., Tan, S.K., 2008b. Comparison of flow patterns in the near wake of a circular cylinder and a square cylinder placed near a plane wall. Ocean Eng. 35, 458–472.
West, G.S., Apelt, C.J., 1997. Fluctuating lift and drag forces on finite lengths of a circular cylinder in the subcritical reynolds number range. J. Fluids Struct 11, 135–158.
Xu, G., Zhou, Y., 2004. Strouhal numbers in the wake of two inline cylinder. Exp. Fluids 37, 248–256.
Zdravkovich, M.M., 1987. The effects of interference between circular cylinders in cross flow. J. Fluids Struct 1, 239–261.
Zdravkovich, M.M., Pridden, D.L., 1977. Interference between two circular cylinders; Series of unexpected discontinuities. J. Ind. Aerodyn 2, 255–270.
Zhou, Y., Yiu, M.W., 2006. Flow structure, momentum and heat transport in a two-tandem-cylinder wake. J. Fluid Mech. 548, 17–48.